Observing the Sun: from start to finish.

PhD dissertation by

Pablo Santamarina Guerrero

Instituto de Astrofísica de Andalucia (IAA-CSIC)

Programa de Doctorado en Física y Matemáticas (FisyMat)
Universidad de Granada

A thesis submitted in fulfillment
of the requirements of the degree of
Doctor of Philosophy

June 18, 2024

PhD thesis supervised by

Dr. David Orozco Suárez
Dr. Julián Blanco Rodríguez

Acknowledgements

Agradecimientos

Resumen

Resumen de la tesis

Summary

Summary of the thesis

CONTENTS

CHAPTER 1

TuMag's design and calibration.

In this chapter we take the first steps of the journey of developing an instrument to observe the Sun. We will define...

The SUNRISE III mission aims to study and stablish the relations and couplings between the phenomena ocurring at different layers of the Sun's surface. With this purpose in mind, three different post-focal instruments were included in the design, each of them responsible of observing at different regions of the spectrum. The SUNRISE UV Spectropolarimeter and Imager (SUSI, **REFERENCIA**), which will observe the spectra between 309 nm and 417 nm; The Sunrise Chromospheric Infrared spectroPolarimeter (SCIP, **REFERENCIA**), which will observe the near-infrared; and lastly, the Tunable Magnetograph (TuMag), which will observe three spectral lines in the visible, at 525.02 nm, 525.06 nm and 517 nm.

The design from scratch of an instrument such as this is very complex. There are many things that have to be meticulously designed and tested which span many fields of expertise, like optics, electronics, software, hardware, or thermal design. To avoid undue extension of this thesis, we will focus on the aspects of the design directly related to the **TO QUE**, that is, regarding the spectral, imaging and polarimetric capabilities of the instrument.

1.1   A brief introduction to spectropolarimeters.

Mirar file:///home/pablo/Downloads/s10509-023-04212-3.pdf.

Spectropolarimeters, as suggested by the name, are devices that measure the spectral and polarimetric properties of light, or in other words, that measure the polarization state of light as a function of wavelength. Their use is widely extended in astrophysics due to the huge amout of information about the light source we can infer from these properties.

In solar physics, it is common to encounter two distinct types of spectropolarimeters, distinguished by their approach to spectroscopy: slit-based spectrographs, such as SUSI and SCIP, and narrow-band tunable filtergraphs, like TuMag. The latter preserve spatial resolution by capturing two-dimensional images of the solar scene at the expense of sacrificing spectral resolution. Conversely, slit-based spectrographs provide excellent spectral resolution but have a limited spatial resolution.

Regardless of how spectroscopy is carried out, spectropolarimeters must be able to mea-

sure the polarization state of light. That is, they must be capable of determining the Stokes parameters of the incident light. These four parameters, usually grouped in a pseudo-vector: $[I, Q, U, V]$, were defined by Stokes in Stokes (1851) as a mathematical formalism to completely define to polarization state of light. The first parameter, I, represents the total intensity; Q and U provide information about the intensity of linearly-polarized light, at 0º and 90º, respectively; and lastly, V, accounts for the intensity of circularly polarized light.

Excellent polarimetric sensitivity and spectral resolution are wasted if the optical capabilities of the instrument are not up to par. The design of these instruments must achieve diffraction-limited imaging, with a signal-to-noise ratio ensuring a polarimetric sensitivity of 1000 (typically), and the best spatial resolution the telescope allows, all without sacrificing spectral resolution and accomplishing this in the shortest possible time.

When designing the instrument, one must balance these three properties: spectral, optical, and polarimetric capabilities, trying to improve the performance in all of them without sacrificing too much. In the following sections, we will delve into each of these aspects in more detail.

1.1.1 Spectroscopy

Narrow-band tunable spectrographs play a significant role in this thesis. They will be extensively discussed in this chapter, particularly in relation to the design and calibration of TuMag, and again in Chapters 2 and 3 when addressing TuMag's pipeline and the correction of data produced by these instruments. Therefore, for the sake of simplicity, we will focus exclusively on this type of spectrographs from this point onward.

CAMBIAR ESTO.

Fabry-Pérot Interferometers (FPIs), also known as etalons (used interchangeably), represent one of the most prevalent forms of narrow-band tunable spectrographs. Composed by a resonant optical cavity formed by two distinct optical media, these devices allow only the passage of light with wavelengths corresponding to constructive interference within the cavity.

The transmission profile of an etalon, being produced by an interference phenomenon, is characterized by a series of narrow and periodic transmission peaks. The wavelengths at which this resonance peaks are located, their width, and their separation are determined solely by the physical properties of the etalon. In fact, it is not difficult to demonstrate (Bailén et al., 2019) that a resonant cavity produces a periodic transmission profile, with maxima occurring at a wavelength λ such that:

REVISAR -> VÁLIDO PARA TELECENTRIC??

$$\lambda = \frac{2nd \cos \theta}{m} \ , \tag{1.1}$$

where n is the refractive index of the medium inside the cavity, d is the distance between the mirrors, θ is the angle of incidence of the incoming light ray and m is the interferential order ($m \in \mathbb{Z}$).
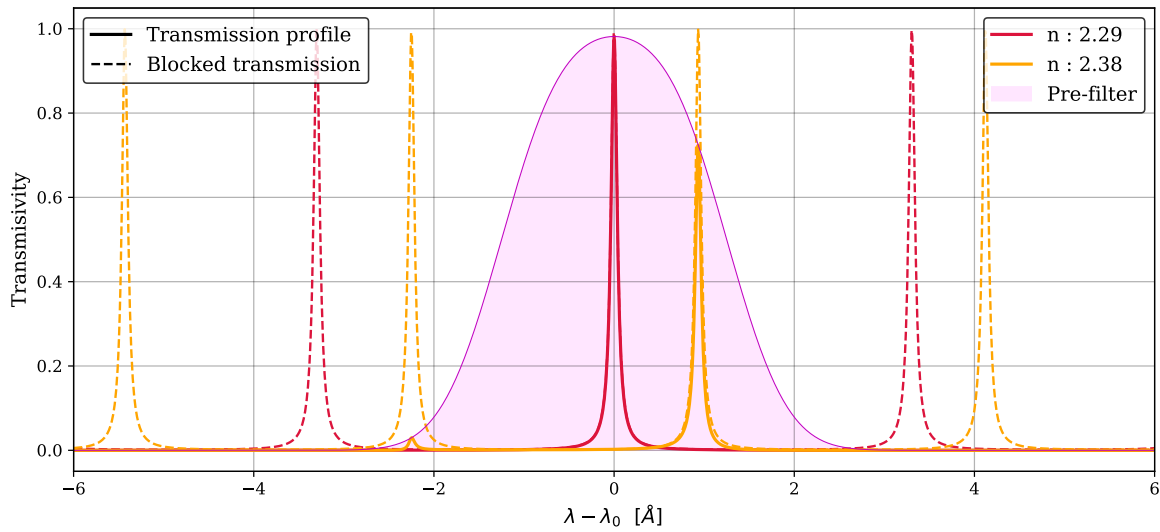
Figure 1.1 Transmission profiles of the same etalon with varying refractive indices (n). The dashed lines represent the original transmission profile, while the solid lines indicate the portion of the transmission profile that passes through the order-sorting pre-filter (shaded purple area).

With Eq. (1.1) in mind, it is clear that an etalon allows for tuning the wavelengths of the transmission peaks by either changing the distance between the mirrors or by altering the refractive index. Although changing the angle of incidence also results in a wavelength shift, it introduces other issues, such as ghost images or profile broadening in telecentric configurations, among other effects. Consequently, the angle is not used for wavelength tuning.

To tune to a single wavelength (or a very narrow band around it), it is necessary to isolate one transmission peak (main order). This is typically achieved by using a pre-filter that only allows light with wavelengths near the desired measurement region to pass through. This ensures that no light reaches the etalon that could pass through it due to interference orders other than the main one (secondary orders).

Figure 1.1 shows a simulation of the spectral behavior of this optical setup. The order-sorting pre-filter is shown with a shaded purple area and the unaltered transmission profile of the etalon is shown in dahsed lines for different values of the refractive index. In solid lines, the resulting transmission profile is shown, that is, the transmission allowed through both the pre-filter and etalon at the same time.

In reality, the spectral and optical properties of FPIs can be quite complex and are influenced not only by their physical characteristics but also by their optical configuration, whether collimated or telecentric. In Chapter 2, we provide a detailed overview of the properties of each configuration, their differences, and the challenges involved in using these devices for data correction.

1.1.2 Imaging

Aquí que va? PSFs Phase diversity?

1.1.3 Polarimetry

XIXA.
    Polatimetros, IQUV bien. Etc.
    S/N y eficiencia.

1.1.4 What for? Zeeman effect.

1.2 The Tunable magnetograph: TuMag

TuMag is a wavelength-tunable spectropolarimeter capable of probing the line-of-sight velocity ($v$los) and the vector magnetic field ($\vec{B}$) in the photosphere and the low chromosphere. This means that TuMag must be able to switch between different spectral lines and measure the full stokes vector at each observed wavelength.

    TuMag's design and properties are a direct consequence of the scientific purpose for which it has been conceived and its requirements.

1.2.1 Optical design and image quality.

1.2.2 Spectral capabilities

As a spectrograph, TuMag is able to tune the wavelength of the measurements through a Fabry-Pérot interferometer (FPI), and select between three different spectral lines through the different pre-filters located on the filter wheel.

    The FPI, or etalon, is a $LiNbO_3$-based ...

1.2.3 Polarimetric capabilities

1.3 Calibration of TuMag

Operation and data reduction.

2.1   TuMag's Pipeline

2.1.1   Darks and flat fields

2.1.2   Blueshift

2.1.3   Demodulation and dual beam

2.1.4   Cross Talk

CHALLENGES IN DATA REDUCTION. ETALON CAVITY MAP.

3.1 Etalon transmission profile

The intensity distribution observed at the focal plane of any etalon-based instrument tuned to a wavelength λ_s obeys the following expression (Bailén et al., 2019):

$$
I\left(\xi, \eta; \lambda_s\right) = g(\xi, \eta) \int_0^\infty T(\lambda) \iint O\left(\xi_0, \eta_0; \lambda\right)
$$

$$
S\left(\xi_0, \eta_0; \xi, \eta; \lambda - \lambda_s\right) \mathrm{d}\xi_0 \, \mathrm{d}\eta_0 \mathrm{d}\lambda, \quad (3.1)
$$

where ξ, η are the coordinates in the image plane, $T(\lambda)$ accounts for the presence of an order-sorting pre-filter, $O\left(\xi_0, \eta_0; \lambda\right)$ represents the brightness distribution of the observed object at the point $\left(\xi_0, \eta_0\right)$, and $S\left(\xi_0, \eta_0; \xi, \eta; \lambda - \lambda_s\right)$ accounts for the imaging response of the instrument when tuned at the wavelength λ_s. The latter coincides with the point spread function (PSF) of the instrument when the optical response is invariant against translations. In such a case, we can substitute the last two integrals by the convolution operator, but this is not strictly true in etalon-based instruments, where the response varies pixel to pixel either because of etalon irregularities or because of variations in the illumination across its clear aperture. We have included a new parameter, $g(\xi, \eta)$, that does not appear in the original work by Bailén et al. (2019) since pixel-to-pixel differences in the detectors' sensitivity are not considered in the original expression. Therefore, $g(\xi, \eta)$ represents a spatial gain factor that accounts for these wavelength independent pixel-to-pixel intensity fluctuations occurring in the focal plane.

As a first approximation, we assumed a spatial dependence of the imaging response in the form of a Dirac delta in order to simplify the equations. If we let the imaging response follow the expression

$$
S\left(\xi_0, \eta_0; \xi, \eta; \lambda - \lambda_s\right) = \delta(\xi_0 - \xi, \eta_0 - \eta)\Psi(\xi, \eta, \lambda - \lambda_s), \quad (3.2)
$$

where $\Psi\left(\xi, \eta; \lambda - \lambda_0\right)$ is the transmission profile of the etalon, Eq. (3.1) can be simplified

as

$$I\left(\xi, \eta; \lambda_s\right) = g(\xi, \eta) \int_0^\infty T(\lambda) O\left(\xi, \eta; \lambda\right) \Psi\left(\xi, \eta; \lambda - \lambda_s\right) d\lambda. \quad (3.3)$$

The transmission profile has a spatial dependence across the image that arises naturally from the different illumination of the etalon across the FoV in the collimated configuration and from the direct mapping of the local inhomogeneities into the detector in the telecentric configuration.

Although, in practice, it is not often possible to fully characterize the pre-filter, we assumed it has a rectangular shape centered at the wavelength of the observed spectral line (λ_0) and a width of $2\Delta\lambda$ such that only one order of the etalon passes through. We note that including a different shape of the pre-filter in the current model is straightforward, provided it can be modeled analytically or even numerically. With this consideration, equation (3.3) can be written as follows:

$$I(\xi, \eta; \lambda_s) = g(\xi, \eta) \int_{\lambda_0 - \Delta\lambda}^{\lambda_0 + \Delta\lambda} O(\xi, \eta; \lambda) \Psi(\xi, \eta; \lambda - \lambda_s) d\lambda. \quad (3.4)$$

The explicit shape of Ψ is different depending on the optical configuration of the instrument, that is, collimated or telecentric.

3.1.1 One device, two configurations

file:///home/pablo/Downloads/s10509-023-04212-3.pdf

3.1.1.1 Collimated configuration

Collimated mounts are characterized by having the etalon located at the pupil plane and therefore receive a collimated beam from each point of the observed object. In this setup, light coming from any point of the object will fall upon the same area of the etalon. Consequently, any local defects on the etalon crystals or on the plates' parallelism is averaged all over the clear aperture, thus making the optical quality constant along the FoV. However, the angle of incidence of the light beam varies along the FoV, thus shifting the transmission profile.

The transmission profile for an ideal collimated etalon tuned at wavelength λ_s takes the following form:

$$\Psi^{\lambda_s}(\lambda, \theta) = \frac{1}{1 + F \sin^2 a_s(\lambda, \theta)}, \quad (3.5)$$

where

$$a_s(\lambda, \theta) = \frac{2\pi}{\lambda} nd \cos\theta, \quad (3.6)$$

with the subscript s indicating that the etalon is tuned at the wavelength λ_s.

The shape of the transmission profile depends on its physical properties. Firstly, the width of the resonance peaks is determined by the parameter F, $F \equiv 4R(1 - R)^{-2}$, which depends exclusively on the reflectivity R of its mirrors. Secondly, the spectral behavior of

the transmission profile is governed by $a_s(\lambda, \theta)$, which is a function of the refractive index of the etalon cavity, n; the distance between mirrors, d; and the angle of the incident beam, θ.

Local defects in the collimated configuration are averaged out, which means that d and n respectively represent the mean values of the thickness and refractive index across the clear aperture of the FPI. Yet, they produce a broadening of the transmission profile and worsen the optical quality of the instrument. The differing angles of incidence over the FoV produce shifts of the transmission that vary quadratically with θ.

3.1.1.2 Telecentric configuration

In the telecentric configuration, the etalon is placed very close to an intermediate focal plane, while the pupil is focused at infinity. This way, the etalon is illuminated by cones of rays that are parallel to each other and reach different sections of the interferometer. Local inhomogeneities (defects or cavities) on the etalon produce differences in the transmission profile across the FoV, which are directly mapped into the image plane. This means that the optical response and the transmission profile shift locally on the image sensor.

The transmission profile of the etalon tuned at a wavelength λ_s is, in this case, given by (Bailén et al., 2021):

$$\Psi^{\lambda_s}(\lambda) = \Re e\left[E(a_s(\lambda, n, d, \theta), b)\right]^2 + \Im m\left[E(a_s(\lambda, n, d, \theta), b)\right]^2, \tag{3.7}$$

with $E(a, b)$ being:

$$E(a, b) = 2\sqrt{\tau}\left\{\int_0^1 \frac{\varrho \cos\left(a\left[1 - b\varrho^2\right]\right)}{1 + F\sin^2\left(a\left[1 - b\varrho^2\right]\right)}d\varrho + \right.$$
$$\left. i\frac{1 + R}{1 - R}\int_0^1 \frac{\varrho \sin\left(a\left[1 - b\varrho^2\right]\right)}{1 + F + \sin^2\left(a\left[1 - b\varrho^2\right]\right)}d\varrho\right\}, \tag{3.8}$$

where τ is the transmission factor of the etalon at normal incidence, ϱ is the radial coordinate of the pupil normalized to the pupil radius of the instrument, a is defined by Eq. (3.6) and b is given by

$$b = \frac{1}{8(nf\#)^2}. \tag{3.9}$$

This parameter accounts for the contribution of the focal ratio, $f\#$, and has an impact on the spectral resolution and the apodization of the pupil as seen from the etalon (Beckers, 1998). Thus, the resolution is now affected by both F and $f\#$, through the parameters a and b.

Contrary to the collimated case, a now has an explicit dependence on the spatial coordinates of the image plane, as n and d change from pixel to pixel. These variations compose the "cavity error" of the etalon and need to be corrected when employing telecentric configurations.
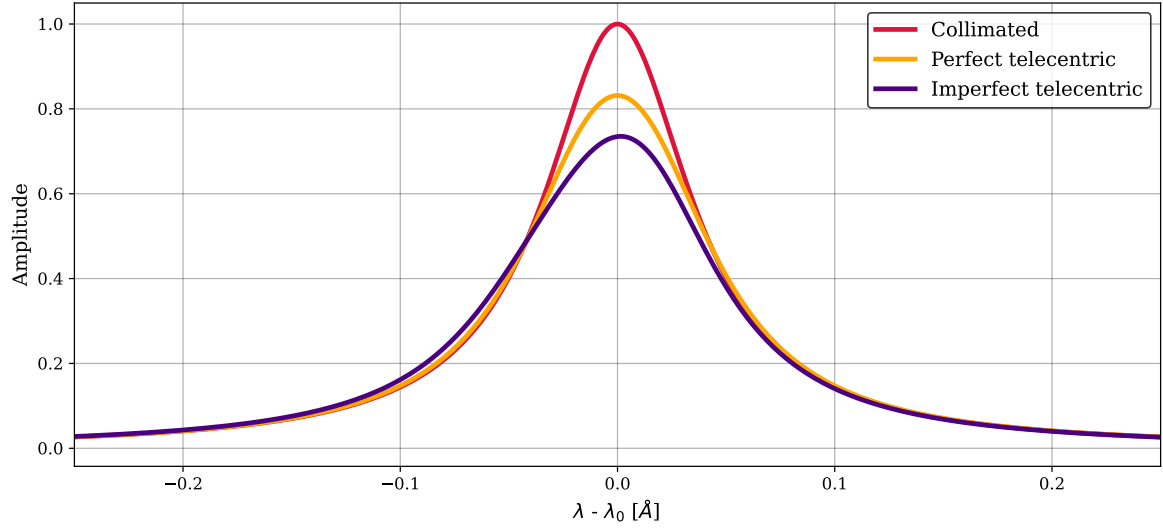
Figure 3.1 Central peak of the etalon's transmission profile for the three different configu-
rations. The parameters of the etalon are $R = 0.92$, $n = 2.29$, $d = 251\,\mu$m, $f\# = 56$, $\theta = 0°$
(collimated and perfect telecentric), and $\Theta = 0.3°$ (imperfect telecentric)

3.1.1.3   Telecentric imperfect configuration

The equations shown in Sect. 3.1.1.2 are valid whenever the incident cone of rays is perpen-
dicular to the etalon mirrors. We refer to this situation hereinafter as "perfect telecentrism".
However, real instruments are likely to present deviations from such an ideal case. These
deviations can be caused by an intentional tilt of the etalon to suppress ghost images on
the detector (Scharmer, 2006), by an accidental tilted angle of incidence caused by devia-
tions from the ideal paraxial propagation of rays within the instrument, or simply because
of misalignment of the optical components. In the three cases, the incident cone of rays
is no longer perpendicular to the etalon, and hence, we consider these scenarios to have
imperfections in the telecentrism degree. One important consequence of the loss of telecen-
trism is an asymmetrization of the transmission profile that must be accounted for when
modeling the instrument response.

The transmission profile in this case is influenced by the angle of incidence of the chief
ray at each point of the clear aperture of the etalon, in addition to the parameters men-
tioned in the previous sections. Unfortunately, the equations for the transmission profile
in these configurations are much more complicated than in the ideal telecentric case, with
no analytical solution to the integrals of the transmission profile. The integrals and their
corresponding derivatives can only be obtained via numerical methods (Bailén et al., 2019).
Figure 3.1 shows the transmission profile corresponding to the three different scenarios we
have considered: collimated illumination of the etalon, perfect telecentrism, and imperfect
telecentrism. The etalon parameters have been selected to coincide with those of SO/PHI's
etalon. In both the collimated and perfect telecentric configurations, a normal incidence
($\theta = 0$) scenario is shown, whereas in the imperfect telecentric case, we assumed an angle

of incidence of the chief ray, Θ, of $0.3°$. The parameter a has been adjusted slightly in order to tune the transmission profile at λ_0.

We observed that the telecentric configurations achieve lower peak transmissions than the collimated case. In addition, the telecentric profiles are wider due to the different incidence angles across the illuminating cone of rays. Such a broadening increases with decreasing f-ratios. Lastly, non-normal incidence of the chief ray in the telecentric configuration further widens and shifts ($\sim$ 4 mÅ for $\Theta = 0.3°$) the profile, making it asymmetrical.

3.1.2 Simulated observations

All the instruments built around the use of an etalon as a wavelength filtering element operate in a very similar way. They scan a spectral line by tuning the etalon (by changing the distance between mirrors and/or modifying the refractive index) to a desired number of wavelengths along the spectral line. At each spectral position, the solar scene is recorded. The measured intensity is approximately given by Eq. (3.4), with the etalon's transmission profile centered at the desired wavelength.

We carried out a series of simulations of a spectral line observation in different conditions. We used the Kitt Peak FTS-Spectral-Atlas as the reference (Brault & Neckel, 1987) and, specifically, the Fe I spectral line at 6173.3 Å. Each observation was composed of N_λ wavelengths, where the measured intensity was recorded. At every wavelength λ_s, the corresponding transmission profile of the etalon Ψ^{λ_s} was computed, and the "observed" intensity $I_{\text{obs},i}^{\lambda_s}$ corresponding to a specific spatial location (ξ, η), represented hereinafter by the pixel i, was calculated using Eq. (3.4). Additionally, we took into account the presence of additive Gaussian noise. This noise does not necessarily respond to any parameter fluctuation within our analytical expressions or photon noise but comes from any unexpected variations that may not have been modeled in the theoretical scheme.

Additionally, we included the presence of defects arising from irregularities or inhomogeneities on either the cavity thickness d, the refractive index n, or from deviations of the angle of incidence θ. In order to simulate this, we introduced a relative perturbation Δa into the etalon equation that accounts for any local deviation of the value of a with respect to its nominal value. This parameter changes from pixel to pixel differently for the collimated and telecentric configurations. In the former, the profile shifts across the FoV only because of the different incidence angles of the light beam on the etalon. In the latter, local variations of n and/or d are mapped directly onto the detector. We also note that variations in the incidence angle must be considered as well when the degree of telecentrism varies along the detector. Analytically, the parameter a at each i-th pixel is given by $a_i' = a\Delta a_i$, where $a = (2\pi/\lambda)nd\cos\theta$ is constant along the FoV.

We let $n_i^{\lambda_s}$ be the noise contribution at the i-th pixel and wavelength λ_s. Thus, the observed intensity at that pixel when the etalon is tuned at λ_s, $I_{\text{obs},i}^{\lambda_s}$ is given by

$$I_{\text{obs},i}^{\lambda_s} = g_i \frac{\int_{\lambda_0-\Delta\lambda}^{\lambda_0+\Delta\lambda} O(\lambda)\Psi^{\lambda_s}(\lambda, \Delta a_i)d\lambda}{\int_{\lambda_0-\Delta\lambda}^{\lambda_0+\Delta\lambda} O(\lambda)\Psi^{\lambda_c}(\lambda, \Delta a_i)d\lambda} + n_i^{\lambda_s}, \tag{3.10}$$
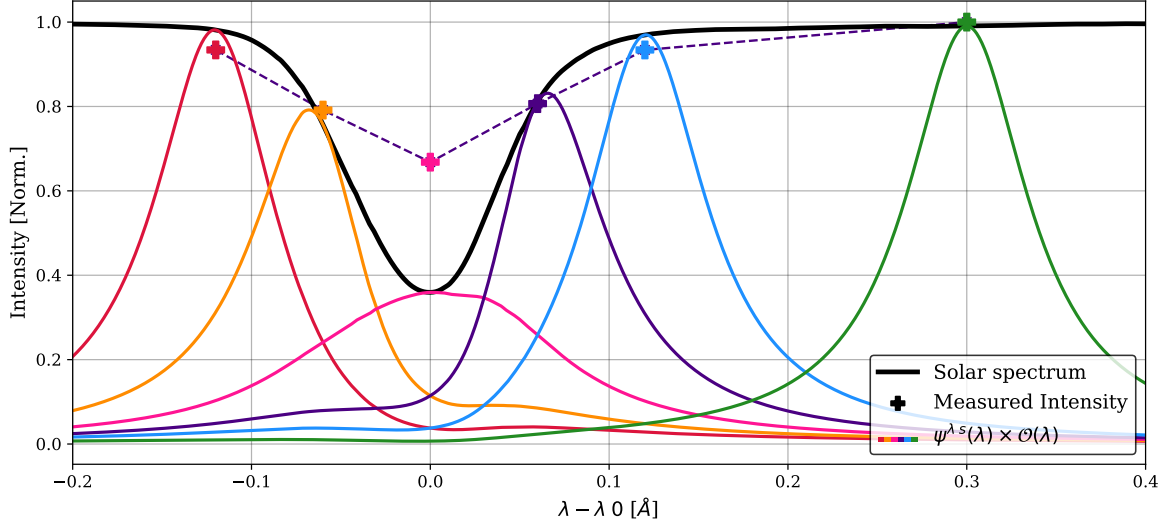
Figure 3.2 Simulated observation of the Fe I spectral line ($\lambda_0 = 6173.3$Å) using a collimated mount and a total of $N_\lambda = 6$ wavelengths that have been equally distributed along the spectral line, with the exception of the continuum measurement (light blue), which is selected at 300 mÅ from the blue of the line core. The measured intensity is the result of computing the value given by Eq. 3.10 at each wavelength and with $g = 1$.

with λ_c being the continuum wavelength. From a practical point of view, the integration limits are set in such a way that only a single resonance (or order) of the etalon is included with the limits, thus, acting akin to the sorting pre-filter commented on previously. We note that the denominator strictly corresponds to the intensity at the continuum of the line in the absence of the transmission profile or if the continuum wavelength is far enough from the spectral line. In any other case, the transmission should be taken into account as well to normalize the observations to the local continuum, which is necessary since we work with relative measurements. An example of a spectral line measurement is displayed in Fig. 3.2.

For both the collimated and telecentric configurations, we modeled etalon and gain imperfections over a 100×100 px^2 image. Pixel-to-pixel variations in the sensor efficiency were modeled following a random spatial distribution, as shown in Fig. 3.3 (top panel). Additionally, we included a set of pixels with very low gain values, which represent a group of dead pixels or dust grains.

We modeled the etalon defects as changes in Δa in such a way that the maximum displacement reaches 3 pm. The spatial distribution of the values of Δa follows an increasing radial distribution, as shown in Fig. 3.3 (bottom panel). Such a spatial distribution coincides with the expected one in collimated etalons due to the change in the incidence angle across the FoV. Telecentric mounts do not exhibit a spatial distribution of their defects such as this, but using the same spatial distribution in the two cases allowed us to compare the performance of the method for both setups in a systematic way. Since Δa accounts for relative perturbations, it is by definition an adimensional parameter. However, to grant it
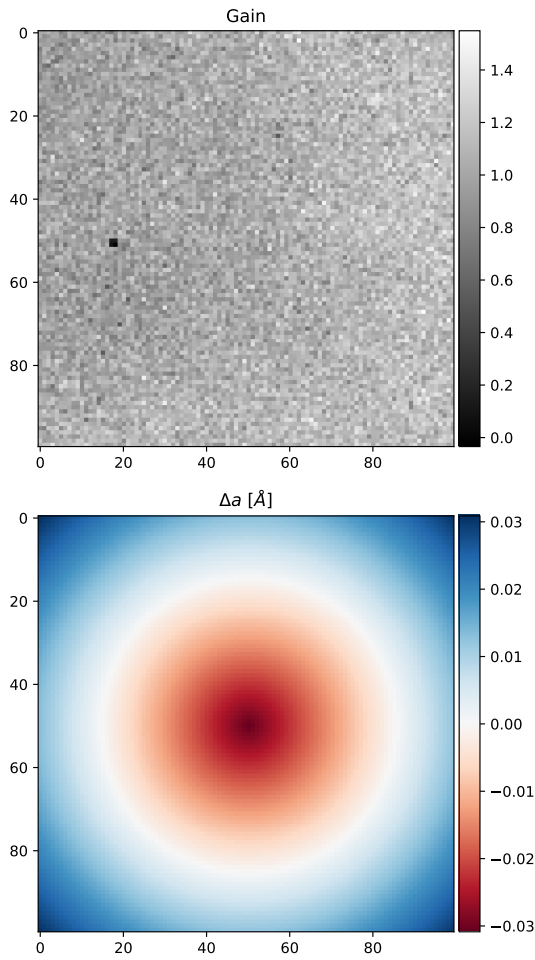
Figure 3.3 Input maps introduced when simulating the observations. The top panel represents the gain generated as white Gaussian noise, with values ranging from 0.8 to 1.2. A dust speck was introduced by creating a group of four pixels with low values of $g = 0.2$ for the gain. The bottom panel shows the spatial distribution of the defects in the etalon. The distribution follows a radial pattern starting from the center of the FoV. The defects vary from 0% deviation to up to $5 \times 10^{-4}\%$, which corresponds to a shift of 3 pm. Both possible directions for the deviations have been considered. The sign of the deviation is negative at the very center, which introduces a redshift, while it is positive at the corners, causing a shift of the profile into the blue.

a physical meaning, we express the values of Δa in Å, representing the associated shift of the transmission profile with respect to the original position determined by a.

3.2   Sunspot observation simulation.

CHAPTER 4

SUMMARY AND CONCLUSIONS

The conclusions are …

APPENDIX A

PROFILE DERIVATVIES

Bibliography

Bailén, F. J., Suárez, D. O., & del Toro Iniesta, J. On fabry–pérot etalon-based instruments. i. the isotropic case. *The Astrophysical Journal Supplement Series* **241**, 9 (2019).

Bailén, F. J., Suárez, D. O., & del Toro Iniesta, J. On fabry–pérot etalon-based instruments. iv. analytical formulation of telecentric etalons. *The Astrophysical Journal Supplement Series* **254**, 18 (2021).

Beckers, J. On the effect of narrow-band filters on the diffraction limited resolution of astronomical telescopes. *Astronomy and Astrophysics Supplement Series* **129**, 191 (1998).

Brault, J., & Neckel, H. Spectral atlas of solar absolute disk-averaged and disk-center intensity from 3290 to 12510 å. *unpublished (tape-copy from KIS IDL library)* (1987).

Scharmer, G. Comments on the optimization of high resolution fabry-pérot filtergraphs. *Astronomy & Astrophysics* **447**, 1111 (2006).

Stokes, G. G. On the composition and resolution of streams of polarized light from different sources. *Transactions of the Cambridge Philosophical Society* **9**, 399 (1851).
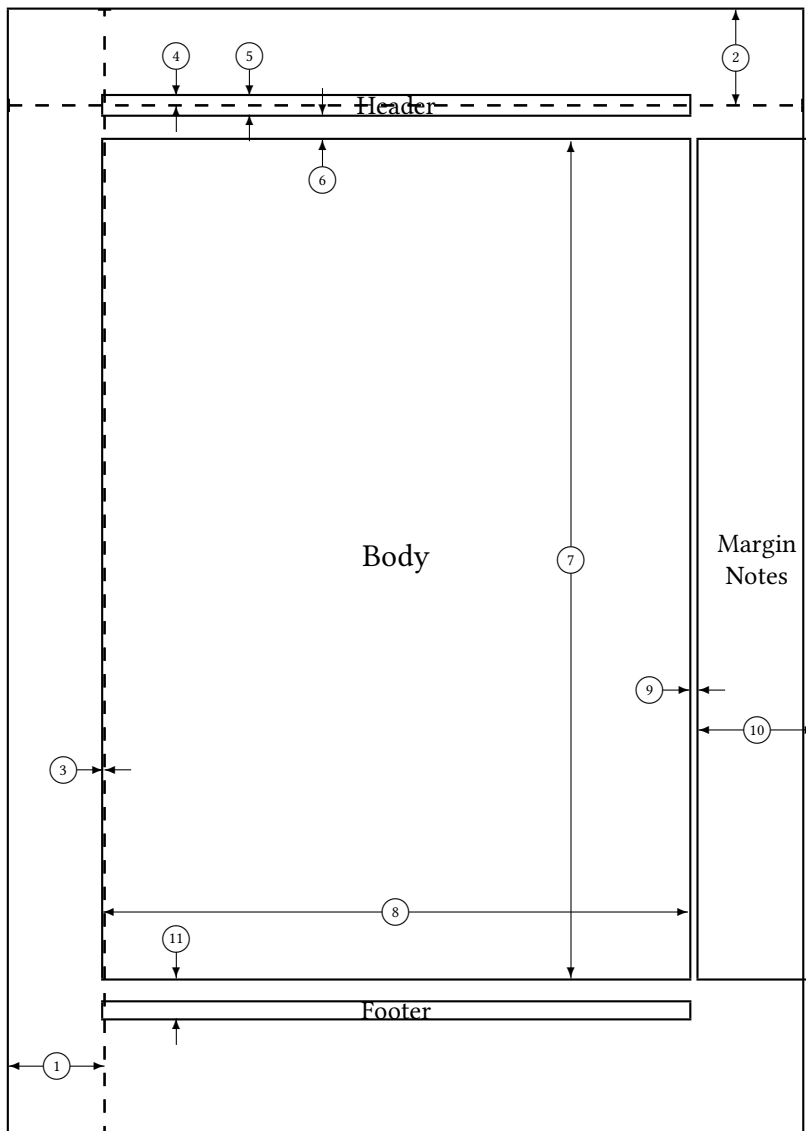
1	one inch + \hoffset	2	one inch + \voffset
3	\oddsidemargin = -1pt	4	\topmargin = -7pt
5	\headheight = 14pt	6	\headsep = 19pt
7	\textheight = 631pt	8	\textwidth = 441pt
9	\marginparsep = 7pt	10	\marginparwidth = 88pt
11	\footskip = 30pt		\marginparpush = 7pt (not shown)
	\hoffset = 0pt		\voffset = 0pt
	\paperwidth = 597pt		\paperheight = 845pt
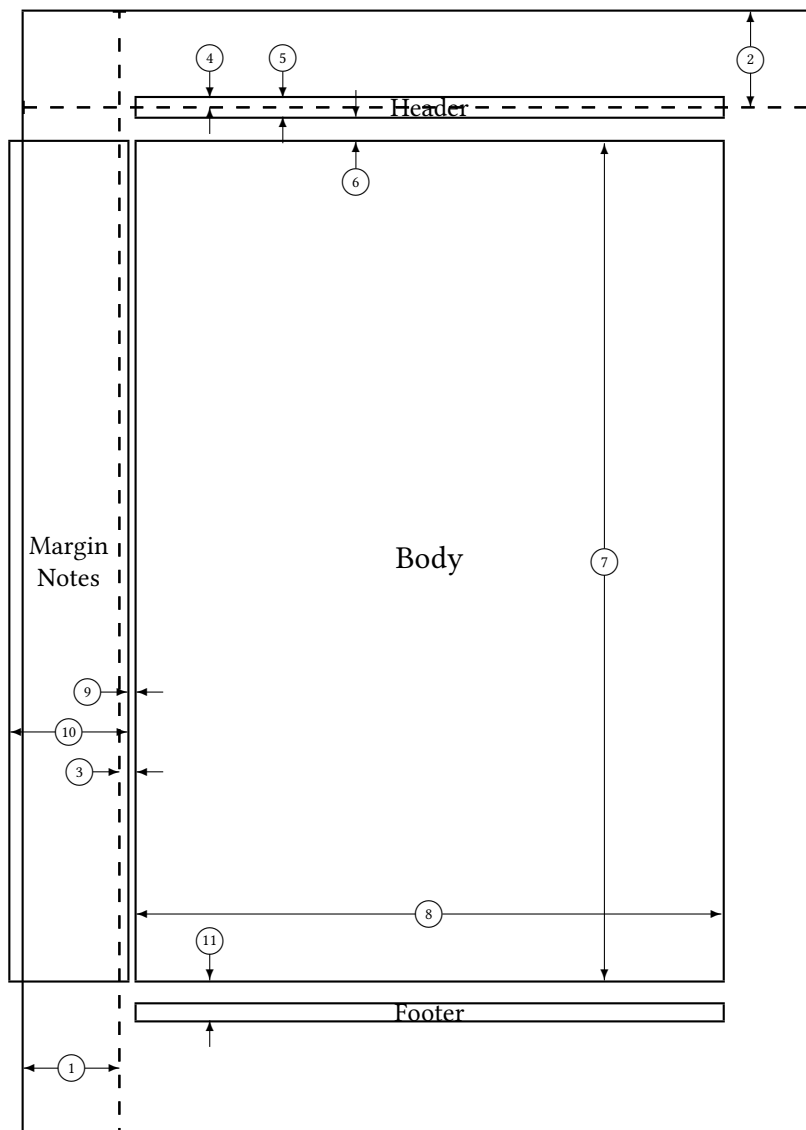
```
1   one inch + \hoffset          2   one inch + \voffset
3   \evensidemargin = 13pt       4   \topmargin = -7pt
5   \headheight = 14pt           6   \headsep = 19pt
7   \textheight = 631pt          8   \textwidth = 441pt
9   \marginparsep = 7pt         10   \marginparwidth = 88pt
11  \footskip = 30pt                 \marginparpush = 7pt (not shown)
    \hoffset = 0pt                   \voffset = 0pt
    \paperwidth = 597pt              \paperheight = 845pt
```